Interpretation®

HOW GAS HYDRATE SATURATION AND MORPHOLOGY CONTROL SEISMIC ATTENUATION: A CASE STUDY FROM THE SOUTH HYDRATE RIDGE

Journal:	*Interpretation*
Manuscript ID	INT-2020-0137.R2
Manuscript Type:	2020-01 Gas Hydrates
Date Submitted by the Author:	17-Nov-2020

Complete List of Authors:	Ji, Aoshuang; Pennsylvania State University, Department of Geosciences Zhu, Tieyuan; Pennsylvania State University, Department of Geosciences Marin-Moreno, Hector; Norwegian Geotechnical Institute Lei, Xiong; China National Oil and Gas Exploration and Development Corporation

Keywords:	hydrates, attenuation, rock physics
Subject Areas:	Case studies

HOW GAS HYDRATE SATURATION AND MORPHOLOGY CONTROL SEISMIC ATTENUATION: A CASE STUDY FROM THE SOUTH HYDRATE RIDGE

Aoshuang Ji[1], Tieyuan Zhu[1,2], Héctor Marín-Moreno[3], Xiong Lei[4]

[1] Department of Geosciences, Pennsylvania State University, USA

[2] EMS Energy Institute, Pennsylvania State University, USA

[3] Norwegian Geotechnical Institute, Norway

[4] Formerly Department of Energy and Mineral Engineering, Pennsylvania State University, USA; Presently China National Oil and Gas Exploration and Development Corporation, China

E-mail addresses: azj64@psu.edu (A. Ji), tyzhu@psu.edu (T. Zhu), hector.marin.moreno@ngi.no (H. M. Moreno), leixiong@cnpcint.com (X. Lei)

ABSTRACT

Prior studies have shown an ambiguous relationship between gas hydrate saturation and seismic attenuation in different regions, but the effect of gas hydrate morphology on seismic attenuation of hydrate-bearing sediments was often overlooked. Here we combine seismic data with rock physics modeling to elucidate how gas hydrate saturation and morphology may control seismic attenuation. To extract P-wave attenuation, we process both the vertical seismic profile (VSP) data within a frequency range of 30 – 150 Hz and sonic logging data within 10 – 15 kHz from three wells in the south Hydrate Ridge, offshore of Oregon (USA), collected during Ocean Drilling Program (ODP) Leg 204 in 2000. We calculate P-wave attenuation using spectral matching and centroid frequency shift methods, and use Archie's relationship to derive gas hydrate saturation from the resistivity data above the bottom simulating reflection (BSR) at the same wells. To interpret observed seismic attenuation in terms of the effects of both gas hydrate saturation and morphology, we employ the Hydrate-Bearing Effective Sediment (HBES) rock physics model. By comparing the observed and model-predicted attenuation values, we infer that: (1) seismic attenuation appears to not be dominated by any single factor, instead, its variation is likely governed by both gas hydrate saturation and morphology; (2) the relationship between seismic attenuation and gas hydrate saturation varies with different hydrate morphologies; (3) the squirt flow, occurring at different compliances of adjacent pores driven by pressure gradients, may be responsible for the significantly large or small attenuation over a broad frequency range.

INTRODUCTION

Gas hydrates are ice-like crystalline compounds of water and gas (mainly methane) molecules, existing naturally in sediments within a limited depth range on the continental margins and permafrost environments at high pressure (>0.6 MPa) and moderately low temperature (<300 K) conditions when methane exceeds its solubility (Brooks et al., 1986; Kvenvolden et al., 1993; Sloan, 1998). Due to its widespread occurrence in the continental margins and permafrost settings, numerous studies, in particular, seismic surveys, have been carried out to investigate the effects of gas hydrate on climate and seafloor stability as well as its important role as a potential energy resource (Dickens, 2003; Bohannon, 2008; Collett et al., 2014a). In recent decades, measurements of seismic velocity, attenuation and gas hydrate saturation have been carried out in the Blake Ridge site off the southeast coast of the United States (Holbrook et al., 1996; Guerin et al., 1999; Hornbach et al., 2008), at the Mallik site in the Mackenzie Delta, Canada (Dallimore and Collett, 2002; Guerin and Goldberg, 2002; Guerin et al., 2005; Bellefleur et al., 2007), in the Nankai Trough, offshore central Japan (Matsushima, 2006), on the western Svalbard continental margin (Carcione et al., 2005; Madrussani et al., 2010), in the Krishna-Godavari (KG) Basin off the eastern coast of India (Jaiswal et al., 2012; Collett et al., 2014b; Shankar, 2016; Jyothi et al., 2017) and in the Gulf of Mexico (Brooks et al., 1986; Phrampus and Hornbach, 2012; Wang et al., 2017).

Generally, gas hydrate growth in the pore space alters the elastic properties of host sediments, allowing us to characterize hydrate-bearing sediments with seismic methods. Previous studies showed that gas hydrate growing in the pore space can stiffen the matrix of the bearing sediments by increasing their bulk and shear moduli, thereby leading to higher P-wave and S-wave velocities (Yuan et al., 1996; Chand et al., 2004; Liu et al., 2020). However, the degree at which the elastic properties are altered depends on both hydrate saturation and morphology (Riedel et al., 2010; Liu and Liu, 2018; Liu et al., 2020). Hydrate morphology can be divided into two main types depending, mainly, on the grain size of the host sediment (Ren et al., 2020). Hydrate growing in fine-grained sediments tends to create particle displacing morphologies such as lenses, nodules, and chunks or veins. In coarse-grained sediments hydrate growth tends to be pore invasive (does not displace the grains) and can be subdivided into (i) pore-floating or pore-filling and (ii) matrix-supporting, including load-bearing, contact-cementing and grain-coating hydrate (Waite et al., 2009; Pan et al., 2019, 2020). For gas hydrate floating in the pore space without any grain contact, the P-wave velocity increases while the S-wave velocity remains almost unchanged due to unaffected shear modulus and minor decrease in bulk density, as the density of gas hydrate is only slightly smaller than that of pore water. When gas hydrate cements grains or acts as part of the load-bearing frame, both the P-wave velocity and the S-wave velocity increase (Chand et al., 2004; Sava and Hardage, 2006; Sahoo et al., 2018, 2019).

Seismic attenuation provides complementary information to velocity on constraining gas hydrate saturation and morphology. However, until now, the investigation of seismic attenuation of hydrate-bearing sediments is scarce partly because good field measurements are limited. As a result, how seismic attenuation varies with gas hydrate properties is still poorly understood. In the field, the effect of gas hydrate saturation on attenuation varies from region to region. For example, in the Mallik field in

Canada, where gas hydrate occurs in subpermafrost occupying up to 60% - 80% of the pore space, the high gas hydrate saturation is associated with high attenuation with Q values of less than 20 for P-waves (Guerin and Goldberg, 2002). A similar observation of high attenuation has been shown in the Nankai Trough in Japan, where gas hydrate locates on the continental margin occupying 20% - 30% of the pore space (Matsushima, 2006). In contrast, the high attenuation is associated with the low gas hydrate saturation observed in the west Svalbard in Norway (Madrussani et al., 2010) and the KG basin in India (Nittala et al., 2017). The measurements of these studies are summarized in Table 1. We find that these measurements exhibit an ambiguous relationship between the attenuation and gas hydrate saturation.

While previous studies attempted to derive the relationship between gas hydrate saturation and seismic attenuation in hydrate-bearing sediments, gas hydrate morphology, which may greatly impact the attenuation in hydrate-bearing sediments, was mostly ignored due to the difficulties of conducting morphology measurements from limited field samples. Therefore, it is challenging to systematically establish a database of gas hydrate morphology from field studies. To explain this gas hydrate morphology-seismic puzzle, rock physics modeling and laboratory measurements have been used. For example, an early study by Lee and Collett (2000) used rock physics modeling to find the relationship between morphology and seismic velocity; Choi et al. (2014) synthesized a non-cementing form of gas hydrate in sandy sediments in the laboratory, measuring the P-wave velocity of the sample during the synthesizing process, and trying to determine gas hydrate morphology at each transition through rock physics modeling. Liu et al. (2020) proposed a joint analysis of P-wave velocity and resistivity to identify hydrate morphology and estimate hydrate saturation in a continuous depth profile. They successfully used the cross plot of P-wave velocity and resistivity to identify fracture-filling gas hydrate-bearing sediments (GHBS) from pore-filling GHBS in the South China Sea based on the observations that fracture-filling gas hydrate-bearing sediments exhibit higher resistivity but lower P-wave velocity than those of pore-filling GHBS in the case of identical hydrate concentration. Recently, Zhan and Matsushima (2018) used the Marín-Moreno's et al. (2017) Hydrate-Bearing Effective Sediment (HBES) model and the Guerin and Goldberg's (2005) model to quantify the attenuation due to a single morphology and multiple morphologies in the Nankai Trough, Japan. Their results confirmed that the occurrence of gas hydrate in different morphologies can better explain the seismic attenuation measurements. However, some questions remain: does the attenuation mechanism behave the same at different hydrate sites and at different hydrate saturation? Our study provides insights into this aspect at a relatively lower hydrate saturation site compared to that of the Nankai Trough in Japan.

In this study, we aim to extend the understanding of how gas hydrate saturation and morphology can alter seismic attenuation and finally elucidate the possible attenuation mechanism in the south Hydrate Ridge. In this work we assume that hydrate growth is pore invasive. We choose high quality vertical seismic profiling (VSP) and sonic logging data to extract P-wave attenuation. We process the VSP data within a frequency range of 30 – 150 Hz and sonic logging data within 10 – 15 kHz from three wells in the south Hydrate Ridge, offshore of Oregon, collected during Ocean Drilling Program (ODP) Leg 204 in 2000 (Tréhu et al., 2004). P-wave attenuation is estimated using spectral matching and centroid frequency shift methods. Different models have

126 been proposed to interpret attenuation measurements on hydrate bearing sediments
127 (Chand and Minshull, 2004; Guerin et al., 2005; Best et al., 2013; Marín-Moreno et al.,
128 2017). To interpret the estimated attenuation from VSP and sonic logging data in terms of
129 the effects of both gas hydrate saturation and morphology, here we employ a frequency
130 dependent HBES rock physics model (Marín-Moreno et al., 2017). The HBES has been
131 recently proven successful in capturing VSP and sonic logging attenuation measurements
132 from natural hydrate bearing sediments in the eastern Nankai Trough (Zhan and
133 Matsushima, 2018). Then we discuss the possible attenuation mechanisms on the gas
134 hydrate sites.
135 Overall, our study helps elucidate the interaction between gas hydrate saturation
136 and morphology in the field, and bridge the gap between gas hydrate and seismic
137 attenuation, which underpins the pivotal role of combining rock physical modeling and
138 field observations in future gas hydrate studies.

139 GEOLOGY AND DATA DESCRIPTION OF THE HYDRATE RIDGE

140 The Hydrate Ridge is located on the Cascadia continental margin which overlies
141 the subduction zone where the Juan de Fuca plates is subducting beneath the North
142 American plate (Figure 1a). Along this margin, two main basins (Cascadia Basin and
143 Gorda Basin), several fans and an accretionary complex have developed. A wide variety
144 of Pleistocene and Holocene turbidites generated most of the deposits in which bottom-
145 simulating reflections (BSRs) are widely recognized. To investigate gas hydrates, a suite
146 of well log data including caliper, gamma ray, resistivity, sonic and VSP was acquired
147 during ODP Leg 204 in the south Hydrate Ridge. The ODP Leg 204 scientific report

(Tréhu et al., 2006c, 2006b) indicated the presence of gas hydrate and revealed its occurrence within turbiditic silty layers. The strong BSR suggests the presence of gas hydrate bearing sediments overlying sediments hosting free gas. An average gas hydrate saturation of ~10% has been estimated in the targeted formations of Leg 204. However, it can reach 20% - 30% in specific locations (e.g. southern summit of the ridge) (Milkov et al., 2003; Tréhu et al., 2004). In this study, we process the VSP (30 – 150 Hz) and sonic logging data (10 – 15 kHz) from three selected sites (Site 1244, 1247 and 1250) (Figure 1b) due to their high data quality to calculate the P wave attenuation over different frequency bands. We obtain hydrate saturation from the resistivity logging data in those wells (Tréhu et al., 2006b) using Archie's relationship (Archie, 1942).

SEISMIC DATA AND ATTENUATION CALCULATION

Field data

Figure 2 shows a two-dimensional (2-D) seismic profile across the location of one of our selected wells. The seismic profile clearly reveals a BSR at 100-150 m depth beneath seafloor (seafloor is at 905 m depth in 1244E well). In this study, we choose high quality near-offset (55 m) VSP data (Figure 3) and monopole sonic data (Figure 4) for attenuation calculation in two frequency bands. Taking 1244E well as an example, VSP data was collected from 85-245 m depth beneath seafloor with a receiver interval of 5 m. In order to make a more reliable calculation, we first apply a median filter to separate the upgoing and downgoing waves, then used a bandpass filter with a frequency of (20-40-80-100 Hz) to filter out noises of downgoing waves. Filtered downgoing waves are windowed with a cosine window (length = 0.025 s) centered at the first peak for later attenuation calculation (Figure 5a). Regarding to sonic data, the transmitter is 108 inches (2.74 m) away from the first receiver and the interval between each receiver is 6 inches (0.15 m). Due to the significant energy concentrating in the relatively lower frequencies (Figure 5b), we apply a bandpass filter (5-6-7-8 kHz) and then a cosine taper window (length = 0.45 ms). Figures 5c and 5d show amplitude spectra of VSP data (Figure 5c) and sonic data (Figure 5d), respectively. The above-mentioned data processing was done using open-source MATLAB software CREWES.

The fact that high frequencies are attenuated more than lower frequencies motivates us to explore the spectra-based methods to calculate seismic attenuation. In this study, we use the spectral matching method proposed by Blias (2012) to estimate VSP attenuation and the centroid frequency method (Quan and Harris, 1997) to estimate sonic attenuation following the workflow as stated below (Figure 6).

Attenuation (1/Q) estimation

Seismic attenuation is often referred to 1/Q, including the scattering and intrinsic attenuation. When the heterogeneities and wavelength are comparable, scattering which is the reflection of the wave in directions other than its original propagation direction will occur. The intrinsic attenuation is the absorbed wave energy converted to heat, often quantified with the inverse of quality factor of the media (Q_{intr}^{-1}). The estimated attenuation which we call effective attenuation (Q_{eff}^{-1}) is the combination of the scattering (Q_{scat}^{-1}) and intrinsic attenuation (Q_{intr}^{-1}), i.e., $Q_{eff}^{-1} = Q_{scat}^{-1} + Q_{intr}^{-1}$. In practice, we are most interested in the intrinsic attenuation which can be compared by calculating its inverse – the quality factor Q for mathematical simplification.

Spectral Matching Method

The spectral matching method is one of the most popular methods for estimating attenuation where data from two receiver depths are selected. Let us assume that a seismic wavelet with amplitude spectrum $S_1(f)$ has an amplitude spectrum $S_2(f)$ after travelling in an attenuating medium for an interval time t. Then, we can describe the seismic attenuation process as:

$$|S_2(f)| = G|S_1(f)|e^{\frac{-\pi f t}{Q}}, \qquad (1)$$

where $S_1(f)$ and $S_2(f)$ are amplitude spectra of downgoing waves at the depth z_1 and z_2, f is the frequency and G represents all the frequency independent amplitude loss in total, including spherical divergence, reflection and transmission loss.

Equation 1 is based on the following assumptions: (1) the source and geophone coupling does no change between the two levels; (2) there is no interference from reflected waves; (3) Q is frequency independent (Tonn, 1991; Harris et al., 1997; Blias, 2012). This formula can be treated as the foundation for most spectral methods to estimate Q. To process VSP data, we use the spectra matching method proposed by Blias (2012). $S_1(f)$ is modified by varying Q until an optimum approximation to $|S_2(f)|$ is obtained:

$$Q_{test} = \min_{Q} \left|\left| |S_2(f)| - G|S_1(f)|e^{\frac{-\pi f (t_2 - t_1)}{Q}} \right|\right|^2, \qquad (2)$$

where G addresses the frequency independent energy loss and can be calculated as:

$$G = \frac{\int_{-\infty}^{\infty} |S_2(f)||S_1(f)| e^{\frac{-\pi f(t_2 - t_1)}{Q}} df}{\int_{-\infty}^{\infty} |S_1(f)|^2 e^{\frac{-2\pi f(t_2 - t_1)}{Q}} df}. \quad (3)$$

Equation 2 was applied to the windowed VSP data described above. The downgoing arrivals at receivers spaced by different intervals (5, 10, 20, 30 m) were tested for Q estimation. We find that the 10 m interval works the best even though they all contain some negative values largely due to scattering or equipment coupling.

Centroid Frequency Shift Method

With observations of significant frequency down-shift in sonic data, we select the centroid frequency shift method (Quan and Harris, 1997) to estimate sonic data attenuation.

With the assumption of Gaussian wavelet, the centroid frequency shift can be linked to wave attenuation as:

$$\int \frac{\pi}{Qv} dl = \frac{f_1 - f_2}{\sigma_1^2}. \quad (4)$$

Where f_1 is the centroid frequency of reference seismogram, f_2 is the centroid frequency of the seismogram at target receivers, and σ_1^2 is the variance of the seismogram at receiver. Therefore, following Quan and Harris (1997), Q between the i_{th} and $(i+1)_{th}$ receiver is defined as:

$$Q = \frac{\pi \sigma_i^2 \Delta t_i}{\Delta f_i}. \quad (5)$$

In equation 5, $\Delta f_i = (f_i - f_{i+1})$ is the centroid frequency difference between the i_{th} and $(i+1)_{th}$ layers, $\Delta t_i = t_i - t_{i+1}$ is the traveltime difference between the two layers, and σ_i^2 is the variance at the i_{th} receiver. Equation 5 is applied to the windowed sonic data described above with the centroid frequencies between 6 kHz to 7 kHz.

VSP AND SONIC ATTENUATION RESULTS

The logging data, including sonic attenuation, of three wells are shown in Figure 7, Figure 8 and Figure 9 for 1244E, 1247B and 1250F, respectively. The gas hydrate zones are identified above the BSR (grey dashed lines) at three wells, which are around 1025 m in 1244E, 976 m in 1247B and 917 m in 1250F below sea level (Tréhu et al., 2006b). In these wells, changes in lithology with depth are likely small, based on the small depth variation of gamma ray (green lines) between 50-70 API. Therefore, we assume that the variation of seismic attenuation with depth in this study area is mainly caused by gas hydrate properties varying with depth.

The gas hydrate saturation is derived from resistivity data using Archie's equation (details in Appendix A). The calculated VSP attenuations range between 0.004 – 0.013 at site 1244E, and 0.004 at site 1247B and 1250F (red dots). They are calculated at certain layers and are generally smaller than the sonic attenuation (black lines in Figure 7, Figure 8 and Figure 9). The uncertainty analysis is implemented using a Monte Carlo method (Riedel et al., 2013; Wang et al., 2017) and errors are illustrated in terms of the standard deviation and 95% confidence interval of average attenuation (details in Appendix B).

ROCK PHYSICS MODELING

To further quantify the effect of gas hydrate saturation and morphology on seismic attenuation, we employ the frequency dependent HBES model (Marín-Moreno et al., 2017) that builds on Best et al.'s (2013) model. The HBES formulation considers that fluid inclusions in the hydrate, which are inclusions of water and/or methane in the hydrate connected to the intergranular pores, can modify the elastic moduli of the hydrate and sediments; fluid inclusions in the hydrate are ellipsoidal, one-sided connected to the intergranular pores, homogeneously distributed in the hydrate, and independent on hydrate morphology; contact-cementing, grain-coating and pore-filling/floating hydrate morphologies as defined by Ecker et al. (1998, 2002). Regarding the application of the HBES to this work, we consider that the pore space above the BSR contains only gas hydrate and water in the pore space and that the hydrate is homogeneously distributed in the pore space.

The two categories of gas hydrate morphology were defined based on whether the hydrate exists adhering to host grains or floating in the pore space and initially deduced from the effect of gas hydrate morphology on the elastic wave velocity (Ecker et al., 1998). The idealized conceptual model of the microstructure of hydrate-bearing sediments is shown in Figure 10.

This model uses the Biot-Stoll poro-elastic theory (Biot, 1956a, 1956b), gas hydrate morphologies as defined by Ecker et al. (1998) and the formulation for squirt flow given by Leurer (1997) to predict seismic attenuation of hydrate bearing sediments. Let us consider the gas hydrate as a compliant composite porous material with inclusions like gas or water, rather than as a solid. The inclusions are a consequence of isolated pockets of gas or water trapped during gas hydrate formation. In this case, the gas hydrate can behave like other microporous, compliant minerals like clay assemblages (Leurer, 1997). When an elastic wave passes through it, the compliant porous host (e.g., host grain framework) and the porous gas hydrate grains create local fluid pressure gradients between the gas hydrate inclusions and the sand frame pores, leading to viscous fluid flow (squirt flow) of water/gas and corresponded wave energy loss. The HBES model allows seismic attenuation to be estimated as a function of frequency, gas hydrate saturation and different combinations of gas hydrate morphologies. A simplified version of the HBES model workflow is shown in Figure 11. The input parameters and symbols of this model are shown in Table C1 and C2 in Appendix C.

COMPARISON AND DISCUSSION

Relation between attenuation and the hydrate properties

Figure 12 shows calculated attenuation from sonic logging data and gas hydrate saturation with depth. Since gas hydrate exists only above the BSR indicated by the grey dashed line in Figure 12 and the VSP data is limited, we only focus on the sonic attenuation above the BSR. Some negative values of attenuation may be resulted from scattering of background or equipment coupling (Matsushima, 2006). The trend between saturation and attenuation is not obvious in Figure 12. We quantify the trend by calculating the correlation coefficients between seismic attenuation and gas hydrate saturation. Small coefficients (-0.34, -0.09 and 0.32 for 1244E, 1247B and 1250F, respectively) imply that there may not be a strong linear relation between seismic attenuation and gas hydrate saturation. In order to see if there is a regional pattern between the seismic attenuation and saturation, we also make a scatter plot of the seismic attenuation and saturation from 1244E (blue circles), 1247B (red circles), and 1250F (yellow circles) in Figure 13. Not surprisingly, there is no clear correlation between gas hydrate saturation and seismic attenuation though we do observe that the attenuation values are more concentrated at lower hydrate saturation and relatively scattered at higher hydrate saturation.

To combine the effect of gas hydrate morphology on the attenuation, we overlay rock physics modeling results on the scatter plot representing different combinations of gas hydrate morphologies between two end-members: cementing and pore-filling hydrate (Marín-Moreno et al., 2017). Then, the modeled attenuations from the HBES model (solid lines) are compared with our calculated attenuations from three wells (Figure 13).

For the modeled results shown as solid lines in Figure 13, we clarify that the fraction attached with pore-filling or cementing means a fraction of the total hydrate saturation, i.e., percentage × hydrate saturation. The attenuation-versus-hydrate saturation curves predicted from the HBES model based on different hydrate morphologies clearly indicate that P-wave attenuation is strongly dependent on gas hydrate morphology. We note that the modeled P-wave attenuation curve with 100% cementing hydrate (red line) appears to capture the upper boundary of calculated sonic attenuations with the increasing of the hydrate saturation, while the modeled P-wave curve with 60% cementing hydrate (yellow line) seems to define the lower boundary of calculated sonic attenuations, in particular at lower saturation. For both the pure pore-filling hydrate (green line) and the multiple morphologies (containing both the pore-filling hydrate and the cementing hydrate) with more pore-filling hydrate (purple and blue lines), the predicted attenuation has a monotonic increase with the saturation. For the multiple morphologies with more cementing hydrate (yellow and black lines), the predicted attenuation can be separated into three stages: (1) at very low saturation (below ~2%), the attenuation increases with the saturation and reaches the peak at around 2%; (2) with saturation increasing from 2% to 10 – 15%, the predicted attenuation decreases gradually; (3) at higher saturations, the predicted attenuation slightly increases. For the pure cementing hydrate model, the predicted attenuation shows the same trend, but the attenuation peak occurs around 6%, then it shows a very smooth decrease at a relatively wider saturation range.

To consider possible frequency effects on attenuation, we compare VSP and sonic attenuations with those modeled at certain layers having gas hydrate saturations of 30%, 24%, 16% and 4% as a function of frequency (Figure 14). Since the VSP attenuations are much smaller and closer for all the three sites, we use the same yellow symbol to display all of them (Figure 14). In general, the VSP attenuation is smaller than the sonic attenuation. Considering the scattering of calculated attenuation from the field data, the modeled results could be treated as a good fit with our measured sonic attenuation. The possible gas hydrate morphologies at some depth in the south Hydrate Ridge in the Cascadia Margin could be around 85% cementing hydrates, which is consistent with the observation of most attenuation data being well represented by hydrate with 60% to 100% cementing morphology (Figure 13).

Discussion

Our results show that the effect of gas hydrate saturation on seismic attenuation can be different: (1) when the percentage of pore-filling hydrates is larger than that of cementing hydrates (see 100%pore-filling, and 20% and 40% cementing curves in Figure 13), in general the attenuation increases with the increasing of saturation; (2) when the percentage of cementing hydrates is larger than pore-filling hydrates (see 60%, 80% and 100% cementing curves in Figure 13), the increase of saturation can lead to a decrease of the attenuation at a certain saturation range controlled by the percentage of cementing hydrate (i.e. more cementing hydrate leads to a decrease of attenuation at a wider saturation range), and then the attenuation increases again as the saturation keeps increasing.

Priest et al. (2006) proposed a reasonable theory for the case with more cementing hydrates: (1) at the first stage (Figure 15a), let us consider a dry sediment specimen with a small volume of adsorbed water, which tends to condense at grain contacts due to surface tension and capillary pressure. When a seismic wave passes through, the generated pressure leads to squirt flow at grain contacts, resulting in energy loss. However, since the amount of adsorbed water is not large enough to fill many grain contact micropores, the energy loss is very small and so minimal attenuation occurs; (2) at the second stage (Figure 15b), hydrate starts to grow in the pore space at grain contacts as a cement, which causes the increase of effective area of the grain contacts followed by more squirt flow. Therefore, more energy could be lost and the attenuation increases rapidly until a critical hydrate saturation; the first two stages are consistent with our results at low saturation (below about 5%); (3) when reaching the third stage (Figure

15c), beyond the critical hydrate saturation, increasing growth of hydrates starts to envelop the host grains and impede the movement of squirt flow, which in turn leads to a reduction in attenuation. However, gas hydrate also has a porous structure (Staykova et al., 2003; Stern et al., 2004), which may still contribute to attenuation caused by squirt flow. Therefore, the attenuation could be close to constant during a certain range of hydrate saturation. In this case, this may correspond to our results at saturations from 5% to 20%; (4) finally, at the fourth stage (Figure 15d), the hydrate starts to create a well-formed interconnected grain-hydrate network resulting in a larger increase in the effective area of the grain contacts, and consequently more energy loss caused by squirt flow, so the attenuation increases again. Our results shown in Figure 13 seems to be consistent with Priest et al. (2006) in that when gas hydrate saturation is pretty low (< 5%), gas hydrate exhibits more likely cementing behavior; once gas hydrate saturation exceeds ~ 5%, the effects of pore-filling and cementing hydrate on seismic attenuation cannot be distinguished. That is why we cannot observe a linear relationship between hydrate saturation and seismic attenuation: effects of hydrate morphology and saturation on seismic attenuation overlap with each other. However, several studies (Tohidi et al., 2001; Yun, 2005; Lee et al., 2010) contradict this, in that cementing behavior cannot be observed at low hydrate saturation (ca. <40%) based on laboratory work. The disagreement may result from the difference between sand specimens most used in the laboratory and the more complicate lithologies in the field, which in our case are clays and silty turbidites. In addition, our study site on the south Hydrate Ridge is located in the subduction zone which could cause more uncertainties than in the laboratory due to the heterogeneity and complexity of the subduction zone setting. Thus, further investigation on the different scales between laboratory and field work combined with rock physics modeling need to be conducted in order to understand the contribution of hydrate to the elastic properties of sediments, particularly seismic attenuation.

Regarding the limitation of the HBES model, as we mention in the previous section, it only assumes two idealized hydrate morphologies, contact-cementing and pore-filling and weights their individual contribution based on their concentration. Though, it could be the case that their average contribution to changes in elastic response of sediments which is not volumetric. In addition, the model assumes initial elliptical macropores and only one aspect ratio of ellipsoidal pores when hydrate forms, whereas in natural environments, it is more likely that a range of aspect ratios are generated.

Fundamentally, estimating seismic attenuation of hydrate-bearing sediments remains challenging. Seismic attenuation comes not only from the intrinsic attenuation of the hydrate-bearing sediments, but also from the scattering due to the heterogeneity of natural sediments. In different hydrate sites, the estimated attenuation values exhibit different ranges even if they were estimated at the same frequency range, as shown in Table 1. Our estimated VSP attenuation values for the Cascadia Margin and the attenuation values at the Nankai Trough (Matsushima, 2006) are lower than those at the Mallik site in Canada (Dvorkin and Uden, 2004) but larger than those in the Krishna-Godavari Basin (KG) in India (Nittala et al., 2017) and offshore Svalbard (Rossi et al., 2007). At different frequency bands, the VSP and sonic attenuation are very different, as shown in Figure 14. However, they are similar to those at the Mallik site in Canada (Dvorkin and Uden, 2004; Pratt et al., 2005). Because of different lithologies in different sites, the dominant attenuation mechanisms can be also different. For example, at the

Mallik site, hydrate saturations up to 60%-80% are inferred in individual sand layers of up to 40 m thick (Bellefleur et al., 2007), and macroscopic squirt flow from elastic heterogeneity in the rock frame elastic moduli may be responsible for the significant attenuation (Dvorkin and Uden, 2004). In the KG Basin in India, there are mainly shale layers, and Nittala et al. (2017) explained the attenuation by accounting for horizontal transverse isotropy. In the Nankai Trough, Zhan and Matsushima (2018) suggested squirt flow due to fluid inclusions in a microporous hydrate and the Biot-squirt (BISQ) mechanism in pore spaces between hydrates and host grains might be the dominant attenuation mechanism in the sonic frequency range, while squirt flow might be the dominant attenuation mechanism in the seismic frequency range. The different thickness of hydrate-bearing sediments may be a factor that influences the attenuations at different hydrate sites. Moreover, gas hydrate can be stored either in marine sediments or permafrost regions, which could result in various hydrate morphologies. We should also note that the free gas coming out from the dissociation of gas hydrate may be captured into a new gas hydrate on its way upwards given proper conditions. Therefore, different lithologies and tectonic settings in different natural hydrate sites can provide significant insights for more comprehensive studies about hydrate morphologies which always show localized characteristics.

Additionally, the laboratory experiments by Priest et al. (2006) indicate that significant seismic attenuation can be caused by the squirt flow due to the adsorbed thin water film between host grains and cementing hydrates. Combining the modeled attenuation using the HBES model with our calculated attenuation from field data, we suggest that squirt flow in the microporous hydrate could play a significant role in seismic attenuation over a broad frequency range in the south Hydrate Ridge. In this study, the VSP attenuation is pretty low compared with the sonic attenuation, which may result from its lower frequency. There are other possible causes, e.g., scattering energy mixing with first arrivals due to strong heterogeneity in the gas hydrate zone, even over shot distance (Tréhu et al., 2004). Moreover, inspired by previous studies mentioned above (Dvorkin and Uden, 2004; Matsushima, 2006; Rossi et al., 2007; Nittala et al., 2017), source-coupling of VSP and sonic equipment could also be a factor. However, since the VSP data is limited and hydrate saturation is only up to about 40%. Hence, for a more comprehensive understanding on the potential role that different seismic frequencies play in regulating the seismic attenuation at gas hydrate sites, complementary studies elsewhere that consider low frequency surface seismic (10 Hz) and/or higher gas hydrate saturations are required.

Compared to the frequent investigation of P-wave attenuation of gas hydrate, lesser quantifications were conducted with S-wave attenuation because the frame rigidity and shear modulus are unaffected if gas hydrate simply fills the space with little grain contact. Future work is needed to fill the gap through comparing different characteristics of P and S-wave in different gas hydrate sites.

CONCLUSION

We have presented a case study using field seismic attenuation measurements and rock physics modeling to investigate the effect of gas hydrate saturation and morphology on seismic attenuation in the south Hydrate Ridge in the Cascadia Margin. We derived seismic VSP and sonic attenuation from field data and interpreted the interrelation between attenuation and gas hydrate saturation and morphology using rock physics modeling, namely HBES hydrate model. The limited data on VSP attenuation shows relatively small values compared to the sonic attenuations. The sonic attenuation shows a scattered distribution with hydrate saturation, suggesting that attenuation is not only controlled by gas hydrate saturation but also likely by morphology. The joint analysis of seismic attenuation measurements and the HBES modeling results demonstrates the theoretical possibility of multiple morphologies coexisting in the pores and the effect of both gas hydrate saturation and morphology in the hydrate-bearing sediments. We propose that in the south Hydrate Ridge (1) cementing hydate may be predominant at low hydrate saturation (<5%), whereas the effects of cementing and pore-filling hydrate cannot be distinguished at relatively higher hydrate saturation; (2) gas hydrate morphology may change with the gas hydrate saturation; (3) squirt flow is responsible for the attenuation changes in the hydrate-bearing sediments at sonic frequencies. Overall, this study provides insights into interpreting the seismic attenuation in the hydrate-bearing sediments using theoretical rock physics models.

ACKNOWLEDGEMENTS

All well log data in this study are available to download in the public data repository of the Ocean Drilling Program (https://mlp.ldeo.columbia.edu/data/odp/leg204/1244E/, https://mlp.ldeo.columbia.edu/data/odp/leg204/1247B/ and https://mlp.ldeo.columbia.edu/data/odp/leg204/1250F/). VSP and sonic data processing and attenuation estimation were done using open-source MATLAB codes from the

Consortium for Research in Elastic Wave Exploration Seismology (CREWES). This research was supported by the Dr. Zhu's startup funding from the Institute of Natural Gas Research at the Pennsylvania State University. We thank Dr. Tao Liu for his help on data processing and Xiaoni Hu for reading the draft. We also thank Drs. Charles Ammon, Sridhar Anandakrishnan and Elizabeth Hajek for their constructive suggestions on the early manuscript. We also appreciate our anonymous reviewers and editors for their invaluable remarks and suggestions.

APPENDICES

Appendix A

Archie's relationship

Archie's equation is used to calculate the hydrate saturation according to resistivity logging profile.

$$S = 1 - (R_t/R) \qquad \text{(A1)}$$

$$R_t = aR_w\emptyset^{-j} \qquad \text{(A2)}$$

where a, j are Archie parameters, $\emptyset$ is the porosity, R_t is the resistivity of formation, R_w is the resistivity of connate water and R is the recorded resistivity with depth. We choose $aR_w = 0.55\ \Omega\ m$ and $j = 1.3$ based on Leg204 gas report (Tréhu et al., 2006a). Note that better saturation calculation could be obtained from recent work (Pan et al., 2019).

Appendix B

Uncertainty analysis of results

Attenuation can be calculated with centroid frequency shift method: $Q = \frac{\pi\sigma_i^2\Delta t_i}{\Delta f_i}$, changes of the centroid frequency Δf_i, velocity, distance (t=distance/velocity) between two receivers and the variance of centroid frequency (σ_i^2) can cause the uncertainty on the attenuation calculations. Since variance is also associated with the frequency, and distance can be measured very accurately, we only consider the uncertainty caused by the frequency and the velocity. To this end, we apply the Monte Carlo method for calculating the attenuation with three receiver pairs (receiver1-6, receiver1-7 and receiver1-8). We randomly select the reasonable frequency range 1000 times, i.e., low frequency and high frequency, which is the same for seismic traces at two receivers. Low frequency randomly changes between 5 – 7 kHz while high frequency randomly changes between 9 – 10 kHz. Arrival time is determined by distance/velocity and velocity is assumed to have an uncertainty of 7.5% (Baron and Holliger, 2010). Therefore, for each interval at each well (1244E, 1247B and 1250F), we can get 3000 Q values (i.e., 1000 × three receiver pairs). To make sure there are enough data samples (>300) for analysis, we filter the interval with more than 300 infinite Q values which are invalid.

The next step is to combine the selected Q values with hydrate saturation at the same depth. In order to quantify the reliability of the results, we plot all the results with their standard deviations shown as different colors (Figure B1), from which we can see most of the results have the standard deviation lower than 0.1. In addition, higher attenuation shows a higher standard deviation which means lower attenuation is much more reliable. However, the standard deviation cannot provide a reliable range of our calculated attenuations. We therefore apply the 95% confidence interval of the mean attenuation to quantify the range. For this purpose, we employ two approaches: (1) Since my sample size is large enough (>100) to use the z-distribution directly, we can simply use the formula: $\bar{x} \pm z\frac{\sigma}{\sqrt{n}}$, where z equals 1.96 after looking for 95% confidence interval; $\bar{x}$ is the sample mean, σ is the sample standard deviation and n is sample size; (2) To verify the 95% confidence interval from approach (1), we use ‘bootstrap’ to calculate the 95% confidence interval again: at each depth, there are n (300<n<3000) valid Q values, we randomly choose 1000 Q values for 3000 times and calculate mean Q values each time, then we can get 3000 mean Q.

The mean Q are normally distributed, and the 95% confidence interval can be easily calculated, which is the same as approach (1) and the results are shown in Figure B2. The black dots in Figure B2 are mean attenuations after resampling selected attenuations at each interval 1000 times, the error bar shows the 95% confidence interval for each mean.

To see the mean attenuation confidence interval in each well and if the resampled results show a similar pattern with Figure 13, we plot these dots in different colors in Figure B3, which still show the same trend and distribution as Figure 13. The modeled results are also plotted in Figure B4, the upper boundary (cementing hydrate) and lower boundary (60% cementing hydrate) restrict the scattering results from the field, the same as Figure 13.

Appendix C

Parameters in the HBES model

The description of input parameters in the HBES model are shown in Tables C1 and C2.

REFERENCES

Archie, G. E., 1942, The Electrical Resistivity Log as an Aid in Determining Some Reservoir Characteristics: Transactions of the AIME, **146**, 54–62.

Baron, L., and K. Holliger, 2010, 9. Analysis of the Velocity Dispersion and Attenuation Behavior of Multifrequency Sonic Logs, *in* Advances in Near-surface Seismology and Ground-penetrating Radar, Society of Exploration Geophysicists, American Geophysical Union, Environmental and Engineering Geophysical Society, 153–166.

Bellefleur, G., M. Riedel, T. Brent, F. Wright, and S. R. Dallimore, 2007, Implication of seismic attenuation for gas hydrate resource characterization, Mallik, Mackenzie Delta, Canada: Journal of Geophysical Research: Solid Earth, **112**, 1–11.

Best, A. I., J. A. Priest, C. R. I. Clayton, and E. V. L. Rees, 2013, The effect of methane hydrate morphology and water saturation on seismic wave attenuation in sand under shallow sub-seafloor conditions: Earth and Planetary Science Letters, **368**, 78–87.

Biot, M. A., 1956a, Theory of Propagation of Elastic Waves in a Fluid-Saturated Porous Solid. I. Low-Frequency Range: The Journal of the Acoustical Society of America, **28**, 168–178.

Biot, M. A., 1956b, Theory of Propagation of Elastic Waves in a Fluid-Saturated Porous Solid. II. Higher Frequency Range: The Journal of the Acoustical Society of America, **28**, 179–191.

Blias, E., 2012, Accurate interval Q-factor estimation from VSP data: Geophysics, **77**, WA149–WA156.

Bohannon, J., 2008, ENERGY: Weighing the Climate Risks of an Untapped Fossil Fuel: Science, **319**, 1753–1753.

Brooks, J. M., H. B. Cox, W. R. Bryant, M. C. Kennicutt, R. G. Mann, and T. J. McDonald, 1986, Association of gas hydrates and oil seepage in the Gulf of Mexico: Organic Geochemistry, **10**, 221–234.

Carcione, J. M., D. Gei, G. Rossi, and G. Madrussani, 2005, Estimation of gas-hydrate concentration and free-gas saturation at the Norwegian-Svalbard continental margin: Geophysical Prospecting, **53**, 803–810.

Chand, S., and T. A. Minshull, 2004, The effect of hydrate content on seismic attenuation: A case study for Mallik 2L-38 well data, Mackenzie delta, Canada: Geophysical Research Letters, **31**, 2–5.

Chand, S., T. A. Minshull, D. Gei, and J. M. Carcione, 2004, Elastic velocity models for gas-hydrate-bearing sediments-a comparison: Geophysical Journal International, **159**, 573–590.

Choi, J. H., S. Dai, J. H. Cha, and Y. Seol, 2014, Laboratory formation of noncementing hydrates in sandy sediments: Geochemistry, Geophysics, Geosystems, **15**, 1648–1656.

Collett, T., J. J. Bahk, R. Baker, R. Boswell, D. Divins, M. Frye, D. Goldberg, J. Husebø,

C. Koh, M. Malone, M. Morell, G. Myers, C. Shipp, and M. Torres, 2014a, Methane hydrates in nature-current knowledge and challenges: Journal of Chemical and Engineering Data, **60**, 319–329.

Collett, T. S., R. Boswell, J. R. Cochran, P. Kumar, M. Lall, A. Mazumdar, M. V. Ramana, T. Ramprasad, M. Riedel, K. Sain, A. V. Sathe, and K. Vishwanath, 2014b, Geologic implications of gas hydrates in the offshore of India: Results of the National Gas Hydrate Program Expedition 01: Marine and Petroleum Geology, **58**, 3–28.

Dallimore, S. R., and T. S. Collett, 2002, Summary and implications of the mallik 2002 gas hydrate production reserch well program: Scientific Results from the Mallik, 1–36.

Dickens, G. R., 2003, CLIMATE: A Methane Trigger for Rapid Warming? Science, **299**, 1017–1017.

Dvorkin, J., and R. Uden, 2004, Seismic wave attenuation in a methane hydrate reservoir: The Leading Edge, **23**, 730–732.

Ecker, C., J. Dvorkin, and A. Nur, 1998, Sediments with gas hydrates: Internal structure from seismic AVO: Geophysics, **63**, 1659–1669.

Ecker, C., J. Dvorkin, and A. M. Nur, 2002, Estimating the amount of gas hydrate and free gas from marine seismic data: GEOPHYSICS, **65**, 565–573.

Guerin, G., and D. Goldberg, 2002, Sonic waveform attenuation in gas hydrate-bearing sediments from the Mallik 2L-38 research well, Mackenzie Delta, Canada: Journal of Geophysical Research, **107**, EPM-1.

Guerin, G., and D. Goldberg, 2005, Modeling of acoustic wave dissipation in gas hydrate-bearing sediments: Geochemistry, Geophysics, Geosystems, **6**, 1–16.

Guerin, G., D. Goldberg, and A. Meltser, 1999, Characterization of in situ elastic properties of gas hydrate-bearing sediments on the Blake Ridge: Journal of Geophysical Research: Solid Earth, **104**, 17781–17795.

Guerin, G., D. Goldberg, and T. S. Collett, 2005, Sonic attenuation in the JAPEX/JNOC/GSC et al. Mallik 5L-38 gas hydrate production research well: GEOLOGICAL SURVEY OF Canada- Bulletin, 1–9.

Harris, P. E., C. Kerner, and R. E. White, 1997, Multichannel estimation of frequency-dependent from VSP data: Geophysical Prospecting, **45**, 87–109.

Holbrook, W. S., H. Hoskins, W. T. Wood, R. A. Stephen, and D. Lizarralde, 1996, Methane hydrate and free gas on the Blake Ridge from vertical seismic profiling: Science, **273**, 1840–1843.

Hornbach, M. J., D. M. Saffer, W. S. Holbrook, H. J. A. Van Avendonk, and A. R. Gorman, 2008, Three-dimensional seismic imaging of the Blake Ridge methane hydrate province: Evidence for large, concentrated zones of gas hydrate and morphologically driven advection: Journal of Geophysical Research, **113**, B07101.

Jaiswal, P., P. Dewangan, T. Ramprasad, and C. A. Zelt, 2012, Seismic characterization of hydrates in faulted, fine-grained sediments of Krishna-Godavari Basin: Full waveform inversion: Journal of Geophysical Research: Solid Earth, **117**.

Jyothi, V., K. Sain, V. Pandey, and A. K. Bhaumik, 2017, Seismic attenuation for characterization of gas hydrate reservoir in Krishna-Godavari basin, eastern Indian margin: Journal of the Geological Society of India, **90**, 261–266.

Kvenvolden, K. A., 1993, Gas hydrates-geological perspective and global change:

Reviews of Geophysics, **31**, 173–187.

Kvenvolden, K. A., G. D. Ginsburg, and V. A. Soloviev, 1993, Worldwide distribution of subaquatic gas hydrates: Geo-Marine Letters, **13**, 32–40.

Lee, J. Y., F. M. Francisca, J. C. Santamarina, and C. Ruppel, 2010, Parametric study of the physical properties of hydrate-bearing sand, silt, and clay sediments: 2. Small-strain mechanical properties: Journal of Geophysical Research, **115**, B11105.

Lee, M. W., and T. S. Collett, 2000, Comparison of elastic velocity models for gas-hydrate-bearing sediments, *in* Geophysical Monograph Series, Vol. 124., 179–187.

Leurer, K. C., 1997, Attenuation in fine-grained marine sediments: Extension of the Biot-Stoll model by the “effective grain model” (EGM): GEOPHYSICS, **62**, 1465–1479.

Liu, T., and X. Liu, 2018, Identification of morphologies of gas hydrate distribution based on amplitude variation with angle analysis: GEOPHYSICS, **83**, B143–B154.

Liu, T., X. Liu, and T. Zhu, 2020, Joint analysis of P-wave velocity and resistivity for morphology identification and quantification of gas hydrate: Marine and Petroleum Geology, **112**, 104036.

Madrussani, G., G. Rossi, and A. Camerlenghi, 2010, Gas hydrates, free gas distribution and fault pattern on the west Svalbard continental margin: Geophysical Journal International, **180**, 666–684.

Marín-Moreno, H., S. K. Sahoo, and A. I. Best, 2017, Theoretical modeling insights into elastic wave attenuation mechanisms in marine sediments with pore-filling methane hydrate: Journal of Geophysical Research: Solid Earth, **122**, 1835–1847.

Matsushima, J., 2006, Seismic wave attenuation in methane hydrate-bearing sediments vertical seismic profiling data from the Nankai trough exploratory well, offshore Tokai, central Japan: Journal of Geophysical Research: Solid Earth, **111**, 1–20.

Nittala, S., K. Sain, and D. Nara, 2017, Seismic vis-a-vis sonic attenuation in gas hydrate bearing sediments of Krishna-Godavari basin, Eastern Margin of India: Geophysical Journal International, **209**, 1195–1203.

Pan, H., H. Li, J. Chen, Y. Zhang, X. Liu, S. Cai, and C. Cao, 2019, Evaluation of gas hydrate resources using hydrate morphology-dependent rock physics templates: Journal of Petroleum Science and Engineering, **182**, 106268.

Pan, H., H. Li, J. Chen, Y. Zhang, S. Cai, Y. Huang, Y. Zheng, Y. Zhao, and J. Deng, 2020, A unified contact cementation theory for gas hydrate morphology detection and saturation estimation from elastic-wave velocities: Marine and Petroleum Geology, **113**, 104146.

Phrampus, B. J., and M. J. Hornbach, 2012, Recent changes to the Gulf Stream causing widespread gas hydrate destabilization: Nature, **490**, 527–530.

Pratt, R. G., F. Hou, K. Bauer, and M. Weber, 2005, Waveform tomography images of velocity and inelastic attenuation from the Mallik 2002 crosshole seismic surveys: GSC Bulletin, **585**, 1–14.

Priest, J. A., A. I. Best, and C. R. I. Clayton, 2006, Attenuation of seismic waves in methane gas hydrate-bearing sand: Geophysical Journal International, **164**, 149–159.

Quan, Y., and J. M. Harris, 1997, Seismic attenuation tomography using the frequency shift: Geophysics, **62**, 895–905.

Ren, X., Z. Guo, F. Ning, and S. Ma, 2020, Permeability of hydrate-bearing sediments: Earth-Science Reviews, **202**, 103100.

Riedel, M., T. S. Collett, P. Kumar, A. V. Sathe, and A. Cook, 2010, Seismic imaging of a fractured gas hydrate system in the Krishna–Godavari Basin offshore India: Marine and Petroleum Geology, **27**, 1476–1493.

Riedel, M., J. J. Bahk, H. S. Kim, N. A. Scholz, D. G. Yoo, W. S. Kim, B. J. Ryu, and S. R. Lee, 2013, Seismic facies analyses as aid in regional gas hydrate assessments. Part-II: Prediction of reservoir properties, gas hydrate petroleum system analysis, and Monte Carlo simulation: Marine and Petroleum Geology, **47**, 269–290.

Rossi, G., D. Gei, G. Böhm, G. Madrussani, and J. M. Carcione, 2007, Attenuation tomography: An application to gas-hydrate and free-gas detection: Geophysical Prospecting, 655–669.

Sahoo, S. K., L. J. North, H. Marín-Moreno, T. A. Minshull, and A. I. Best, 2019, Laboratory observations of frequency-dependent ultrasonic P-wave velocity and attenuation during methane hydrate formation in Berea sandstone: Geophysical Journal International, **219**, 713–723.

Sahoo, S. K., B. N. Madhusudhan, H. Marín-Moreno, L. J. North, S. Ahmed, I. H. Falcon-Suarez, T. A. Minshull, and A. I. Best, 2018, Laboratory Insights Into the Effect of Sediment-Hosted Methane Hydrate Morphology on Elastic Wave Velocity From Time-Lapse 4-D Synchrotron X-Ray Computed Tomography: Geochemistry, Geophysics, Geosystems, **19**, 4502–4521.

Sava, D., and B. A. Hardage, 2006, Rock physics characterization of hydrate-bearing deepwater sediments: The Leading Edge, **25**, 616–619.

Shankar, U., 2016, Gas hydrate saturation from seismic data constrained by log data in the Krishna-Godavari Basin: Journal of Petroleum Exploration and Production

Technology, **6**, 13–23.

Sloan, E. D., 1998, Gas hydrates: Review of physical/chemical properties: Energy and Fuels, **12**, 191–196.

Staykova, D. K., W. F. Kuhs, A. N. Salamatin, and T. Hansen, 2003, Formation of Porous Gas Hydrates from Ice Powders: Diffraction Experiments and Multistage Model: The Journal of Physical Chemistry B, **107**, 10299–10311.

Stern, L. A., S. H. Kirby, S. Circone, and W. B. Durham, 2004, Scanning electron microscopy investigations of laboratory-grown gas clathrate hydrates formed from melting ice, and comparison to natural hydrates: American Mineralogist, **89**, 1162–1175.

Tohidi, B., R. Anderson, M. Ben Clennell, R. W. Burgass, and A. B. Biderkab, 2001, Visual observation of gas-hydrate formation and dissociation in synthetic porous media by means of glass micromodels: Geology, **29**, 867.

Tonn, R., 1991, The determination of the seismic quality factor Q from VSP data: A comparison of different computational methods: Geophysical Prospecting, **39**, 1–27.

Tréhu, A. M., P. E. Long, M. E. Torres, G. Bohrmann, F. R. Rack, T. S. Collett, D. S. Goldberg, A. V. Milkov, M. Riedel, P. Schultheiss, N. L. Bangs, S. R. Barr, W. S. Borowski, G. E. Claypool, M. E. Delwiche, G. R. Dickens, E. Gracia, G. Guerin, M. Holland, J. E. Johnson, Y. J. Lee, C. S. Liu, X. Su, B. Teichert, H. Tomaru, M. Vanneste, M. Watanabe, and J. L. Weinberger, 2004, Three-dimensional distribution of gas hydrate beneath southern Hydrate Ridge: Constraints from ODP Leg 204: Earth and Planetary Science Letters, **222**, 845–862.

Tréhu, A. M., M. E. Torres, G. Bohrmann, and F. S. Colwell, 2006a, Leg 204 synthesis:

gas hydrate distribution and dynamics in the central Cascadia accretionary complex: Proceedings of the Ocean Drilling Program, 199 Scientific Results, **204**.

Tréhu, A. M., G. Bohrmann, M. E. Torres, F. S. Colwell, M. W. Lee, and T. S. Collett, 2006b, Gas Hydrate and Free Gas Saturations Estimated from Velocity Logs on Hydrate Ridge, Offshore Oregon, USA:

Waite, W. F., J. C. Santamarina, D. D. Cortes, B. Dugan, D. N. Espinoza, J. Germaine, J. Jang, J. W. Jung, T. J. Kneafsey, H. Shin, K. Soga, W. J. Winters, and T.-S. Yun, 2009, Physical properties of hydrate-bearing sediments: Reviews of Geophysics, **47**, RG4003.

Wang, J., S. Wu, J. Geng, and P. Jaiswal, 2017, Acoustic wave attenuation in the gas hydrate-bearing sediments of Well GC955H, Gulf of Mexico: Marine Geophysical Research, **39**, 509–522.

Yuan, T., R. D. Hyndman, G. D. Spence, and B. Desmons, 1996, Seismic velocity increase and deep-sea gas hydrate concentration above a bottom-simulating reflector on the northern Cascadia continental slope: Journal of Geophysical Research: Solid Earth, **101**, 13655–13671.

Yun, T. S., 2005, Compressional and shear wave velocities in uncemented sediment containing gas hydrate: Geophysical Research Letters, **32**, L10609.

Zhan, L., and J. Matsushima, 2018, Frequency-dependent P-wave attenuation in hydrate-bearing sediments: A rock physics study at Nankai Trough, Japan: Geophysical Journal International, **214**, 1961–1985.

LIST OF FIGURES

Figure 1. Location of Leg 204 on the South Hydrate Ridge on the Cascadia continental margin which overlies the subduction zone of Juan de Fuca plates thrusting beneath the North American plate. Seismic data is from Sites 1244, 1247 and 1250; black circles represent other drillings; red line shows the surface seismic line crossing site 1244 (Modified after Leg 204 Report, 2006).

Figure 2. Seismic section across Site 1244 where BSR (indicated by arrows) can be recognized at 100 – 150 m depth.

Figure 3. Raw z-component near-offset (55 m) VSP seismic data in (a) 1244E; (b) 1247B; (c) 1250F.

Figure 4. Raw sonic logging data in (a) 1244E; (b) 1247B; (c) 1250F.

Figure 5. (a) Z component of near offset (55 m) VSP downgoing recording after pre-processing; (b) Monopole seismic traces obtained from sonic logging; (c) Spectrum of VSP traces for shallower trace (blue) and deeper trace (red); (d) Spectrum of sonic traces at receiver 1 (blue) and receiver 8 (red).

Figure 6. The data processing procedure for (a) the VSP and (b) the sonic logging to estimate the seismic attenuation.

Figure 7. 1244E well logging data: (a) gamma ray, (b) resistivity, (c) gas hydrate saturation derived from the log of resistivity using Archie’s equation, (d) P-wave velocity and (e) attenuation. The dashed line represents BSR.

Figure 8. 1247B well logging data: (a) gamma ray, (b) resistivity, (c) gas hydrate saturation derived from the log of resistivity using Archie’s equation, (d) P-wave velocity and (e) attenuation. The dashed line represents BSR.

Figure 9. 1250F well logging data: (a) gamma ray, (b) resistivity, (c) gas hydrate saturation derived from the log of resistivity using Archie's equation, (d) P-wave velocity and (e) attenuation. The dashed line represents BSR.

Figure 10. Idealized conceptual illustration of the microstructure of hydrate-bearing sediments. A = Cementing at grains contact; B = Pore-filling hydrates framework.

Figure 11. Simplified workflow of the Hydrate-Bearing Effective Sediment (HBES) model. More detailed descriptions and procedures can be referred to Marín-Moreno et al. (2017).

Figure12. Comparison between the seismic attenuation and gas hydrate saturation above the BSR (grey dotted line) at (a) 1244E, (b) 1247B and (c) 1250F, respectively.

Figure 13. Measured attenuation (dots) and modeled attenuation (lines) as a function of gas hydrate saturation of 1244E (blue circles), 1247B (red circles) and 1250F (yellow circles), respectively. Note that the summation of pore-filling and cementing hydrate adds 100%.

Figure 14. Measured attenuation (dots) and modeled attenuation (lines) of P wave as a function of frequency at (a) 4%, (b) 16%, (c) 24% and (d) 30% gas hydrate saturation. Note that 85%, 90% and 95% cementing refer to the fraction of cementing of the total hydrate saturation, i.e., 85% (or 90%/95%) × hydrate saturation.

Figure 15. Conceptual model of cementing hydrates growing at grain contacts with increasing gas hydrate saturation. (a) Host grains without hydrates; (b) Hydrates growing at grain boundaries; (c) Enveloped grains with hydrates; (d) Interconnected grain-hydrate network (Modified after Priest et al., 2006).

Figure B1. Scattering plot of the seismic attenuation and gas hydrate saturation above the BSR from 1244E, 1247B and 1250F. Different colors represent the standard deviation of P wave attenuation.

Figure B2. Measured mean attenuation (dots) with error bar showing the 95% confidence interval as a function of gas hydrate saturation.

Figure B3. Measured mean attenuation (dots) with error bar showing the 95% confidence interval as a function of gas hydrate saturation for 1244E, 1247B and 1250F, respectively.

Figure B4. Measured mean attenuation (dots) with error bar showing the 95% confidence interval and modeled attenuation (lines) as a function of gas hydrate saturation.

LIST OF TABLES

Table 1. Published and this study's seismic attenuation (Q value is the inverse of the attenuation) for hydrate-bearing sediments.

Table C1. Fixed input parameters used in the HBES model.

Table C2. Case dependent input parameters used in the HBES model.

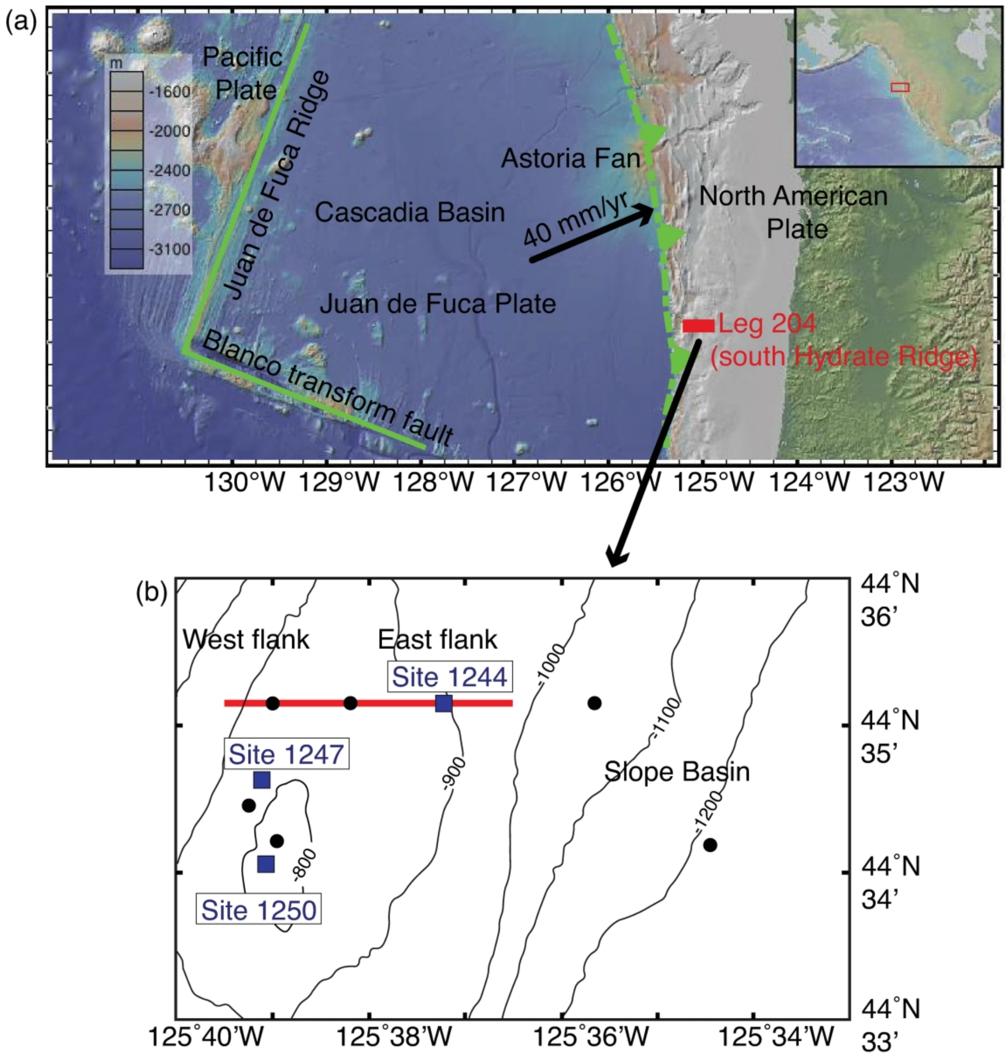

Figure 1. Location of Leg 204 on the South Hydrate Ridge on the Cascadia continental margin which overlies the subduction zone of Juan de Fuca plates thrusting beneath the North American plate. Seismic data is from Sites 1244, 1247 and 1250; black circles represent other drillings; red line shows the surface seismic line crossing site 1244 (Modified after Leg 204 Report, 2006).

269x284mm (300 x 300 DPI)

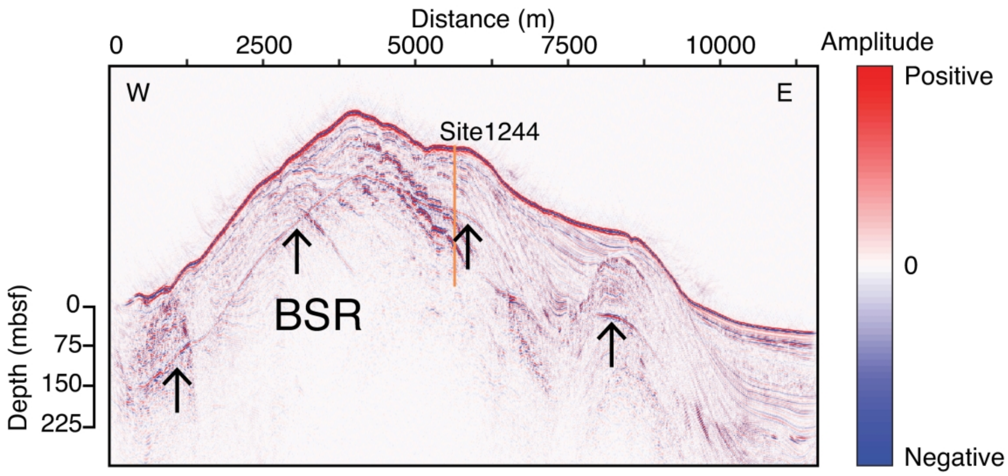

Figure 2. Seismic section across Site 1244 where BSR (indicated by arrows) can be recognized at 100 – 150 m depth.

289x137mm (300 x 300 DPI)

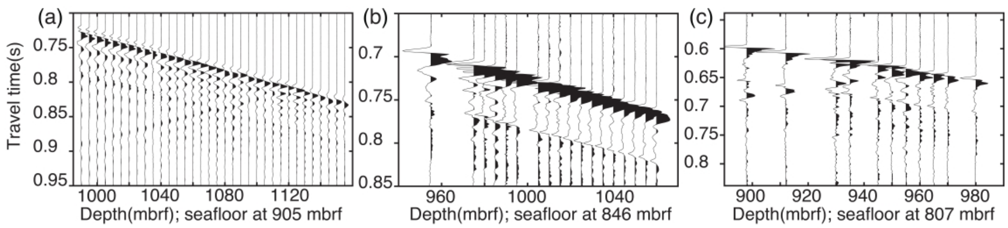

Figure 3. Raw z-component near-offset (55 m) VSP seismic data in (a) 1244E; (b) 1247B; (c) 1250F.

1192x266mm (600 x 600 DPI)

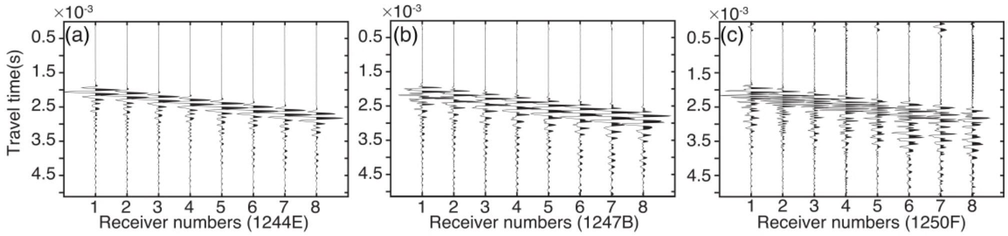

Figure 4. Raw sonic logging data in (a) 1244E; (b) 1247B; (c) 1250F.

1202x290mm (600 x 600 DPI)

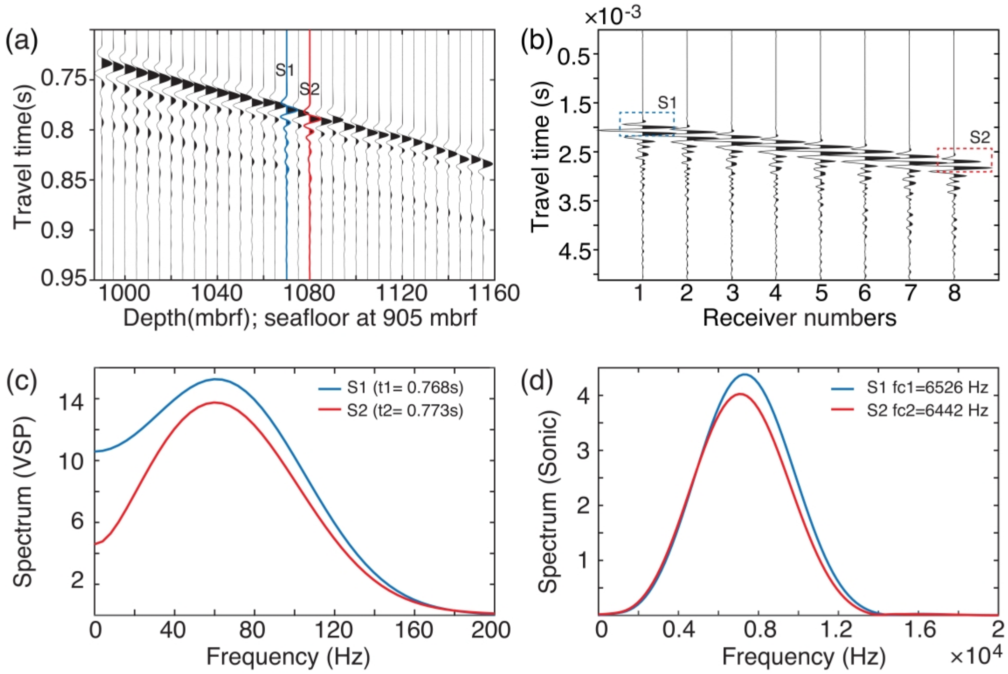

Figure 5. (a) Z component of near offset (55 m) VSP downgoing recording after pre-processing; (b) Monopole seismic traces obtained from sonic logging; (c) Spectrum of VSP traces for shallower trace (blue) and deeper trace (red); (d) Spectrum of sonic traces at receiver 1 (blue) and receiver 8 (red).

1242x839mm (600 x 600 DPI)

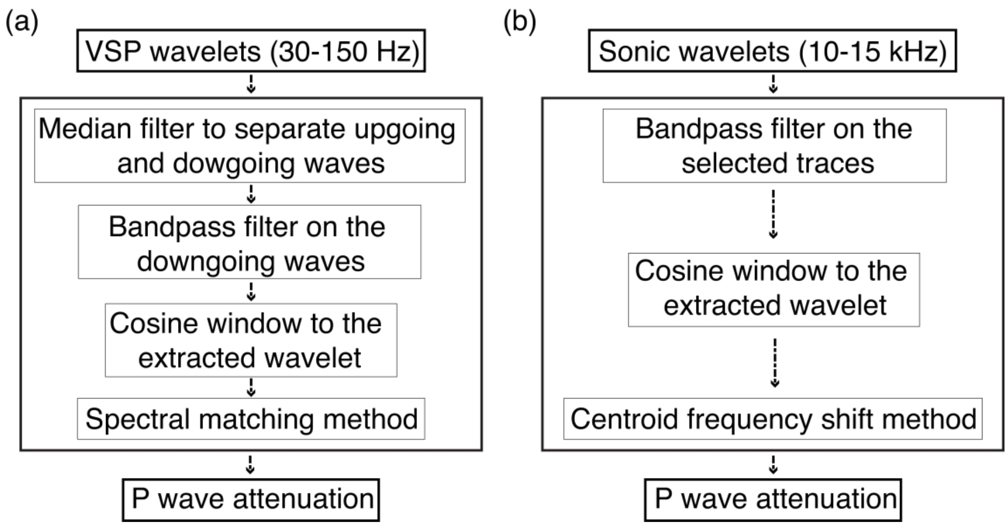

Figure 6. The data processing procedure for (a) the VSP and (b) the sonic logging to estimate the seismic attenuation.

737x380mm (600 x 600 DPI)

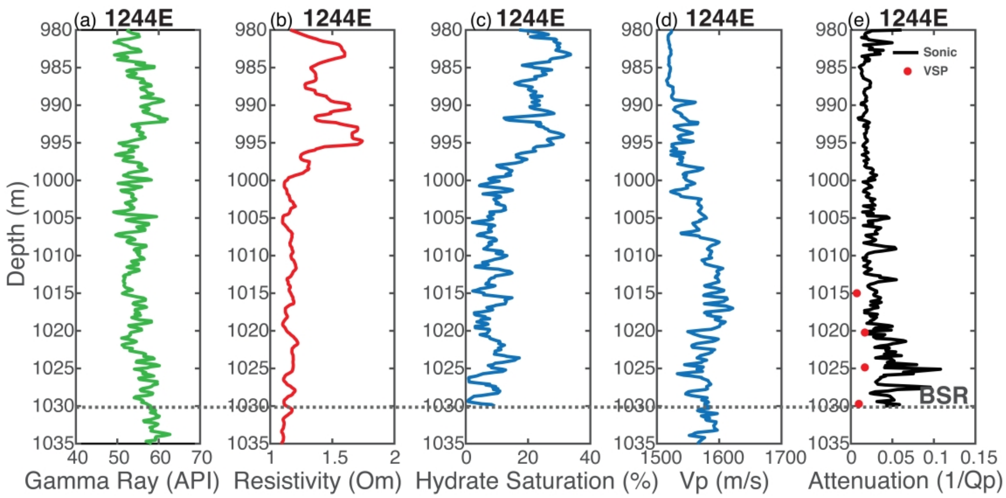

Figure 7. 1244E well logging data: (a) gamma ray, (b) resistivity, (c) gas hydrate saturation derived from the log of resistivity using Archie's equation, (d) P-wave velocity and (e) attenuation. The dashed line represents BSR.

882x435mm (600 x 600 DPI)

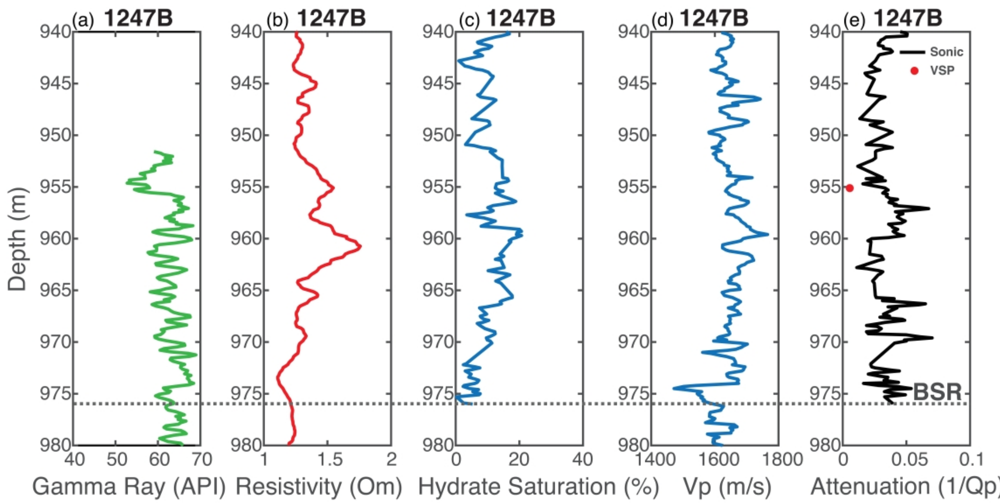

Figure 8. 1247B well logging data: (a) gamma ray, (b) resistivity, (c) gas hydrate saturation derived from the log of resistivity using Archie's equation, (d) P-wave velocity and (e) attenuation. The dashed line represents BSR.

888x443mm (600 x 600 DPI)

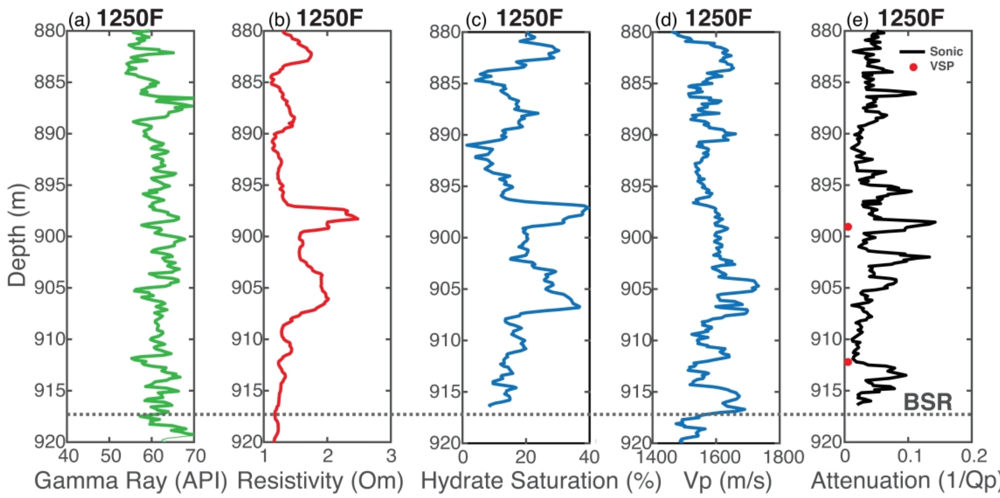

Figure 9. 1250F well logging data: (a) gamma ray, (b) resistivity, (c) gas hydrate saturation derived from the log of resistivity using Archie's equation, (d) P-wave velocity and (e) attenuation. The dashed line represents BSR.

890x441mm (600 x 600 DPI)

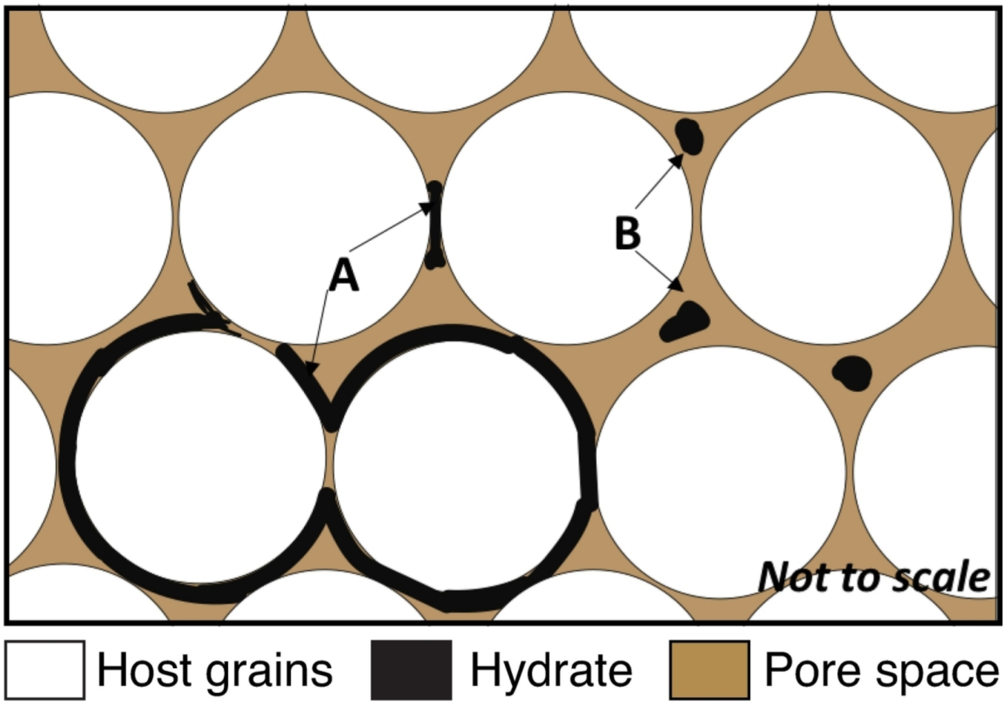

Figure 10. Idealized conceptual illustration of the microstructure of hydrate-bearing sediments. A = Cementing at grains contact; B = Pore-filling hydrates framework.

134x95mm (300 x 300 DPI)

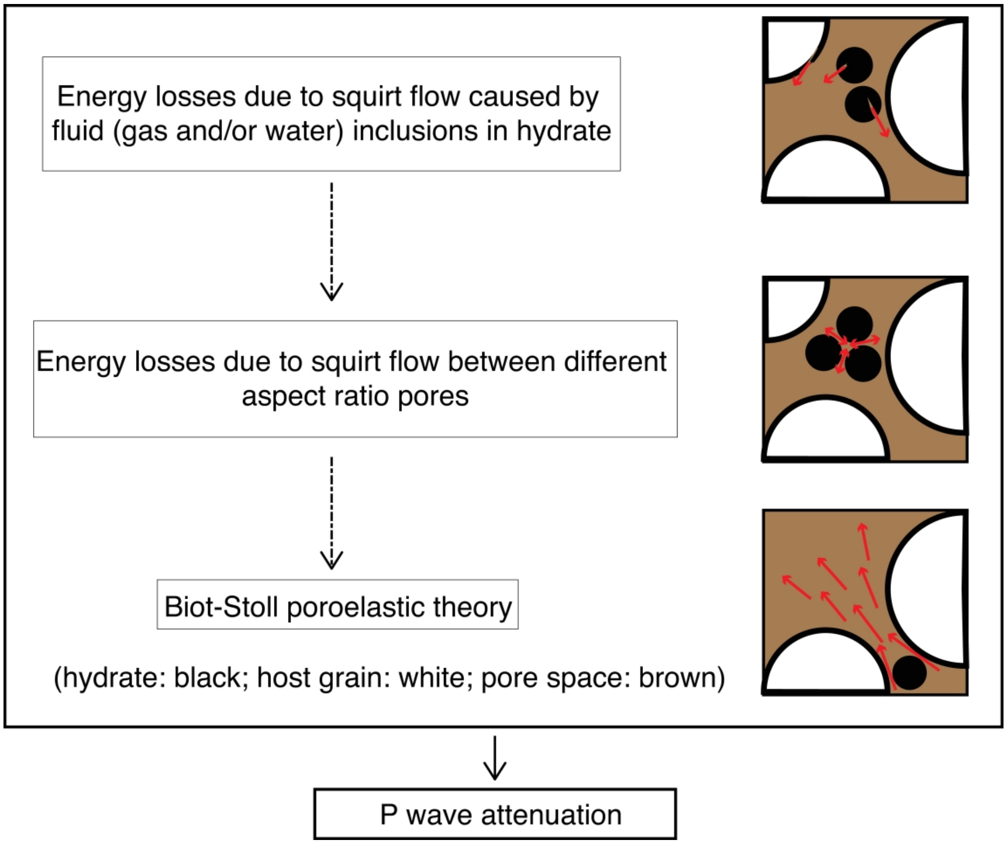

Figure 11. Simplified workflow of the Hydrate-Bearing Effective Sediment (HBES) model. More detailed descriptions and procedures can be referred to Marín-Moreno et al. (2017).

615x515mm (600 x 600 DPI)

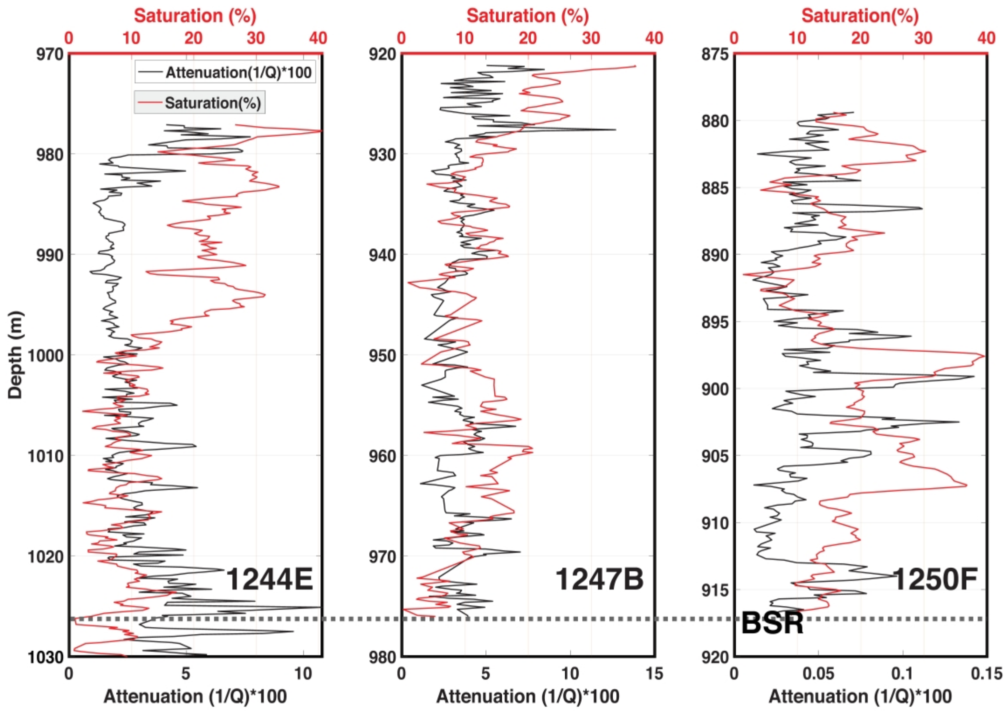

Figure 12. Comparison between the seismic attenuation and gas hydrate saturation above the BSR (grey dotted line) at (a) 1244E, (b) 1247B and (c) 1250F, respectively.

626x443mm (600 x 600 DPI)

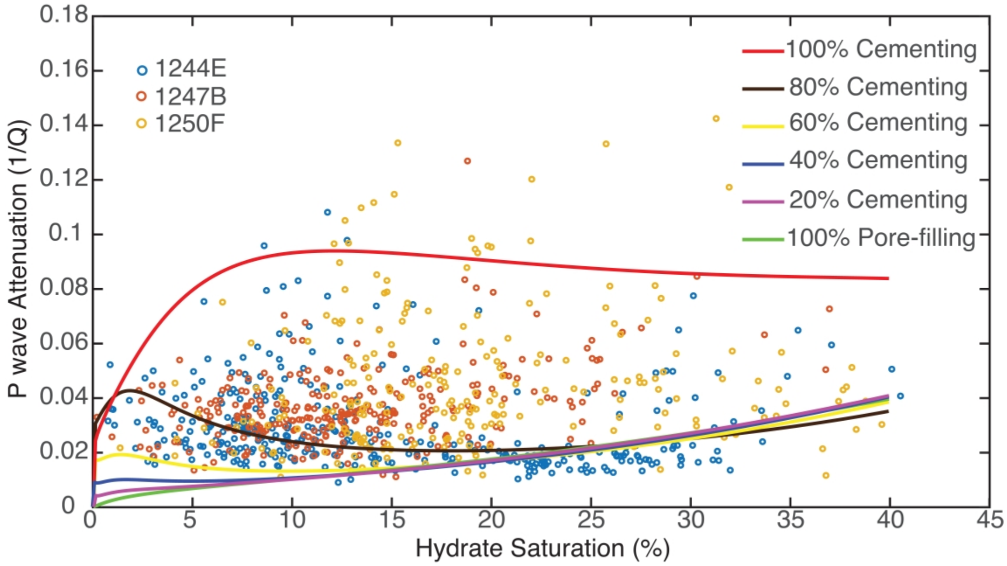

Figure 13. Measured attenuation (dots) and modeled attenuation (lines) as a function of gas hydrate saturation of 1244E (blue circles), 1247B (red circles) and 1250F (yellow circles), respectively. Note that the summation of pore-filling and cementing hydrate adds 100%.

841x479mm (600 x 600 DPI)

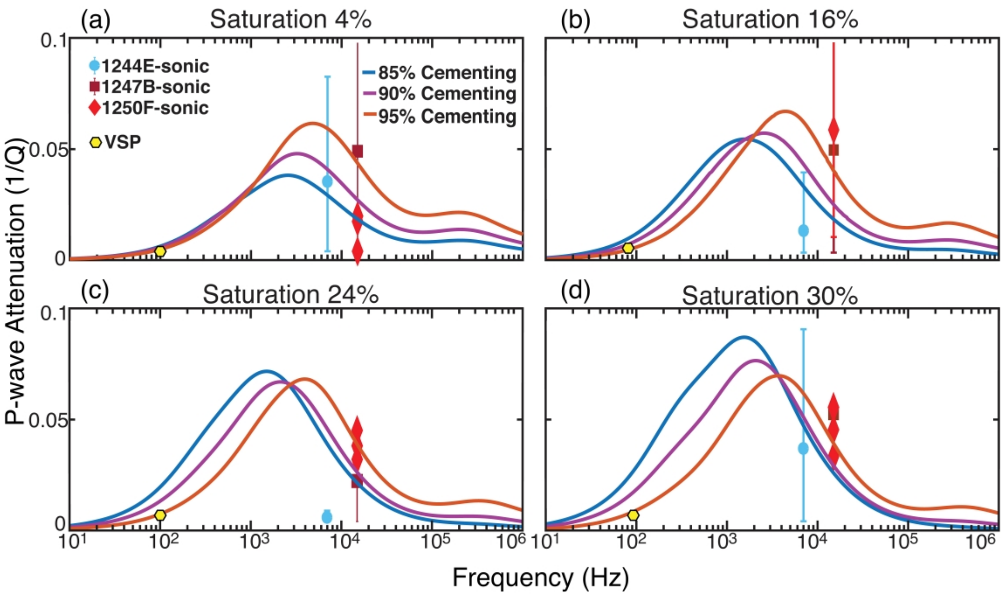

Figure 14. Measured attenuation (dots) and modeled attenuation (lines) of P wave as a function of frequency at (a) 4%, (b) 16%, (c) 24% and (d) 30% gas hydrate saturation. Note that 85%, 90% and 95% cementing refer to the fraction of cementing of the total hydrate saturation, i.e., 85% (or 90%/95%) × hydrate saturation.

817x484mm (600 x 600 DPI)

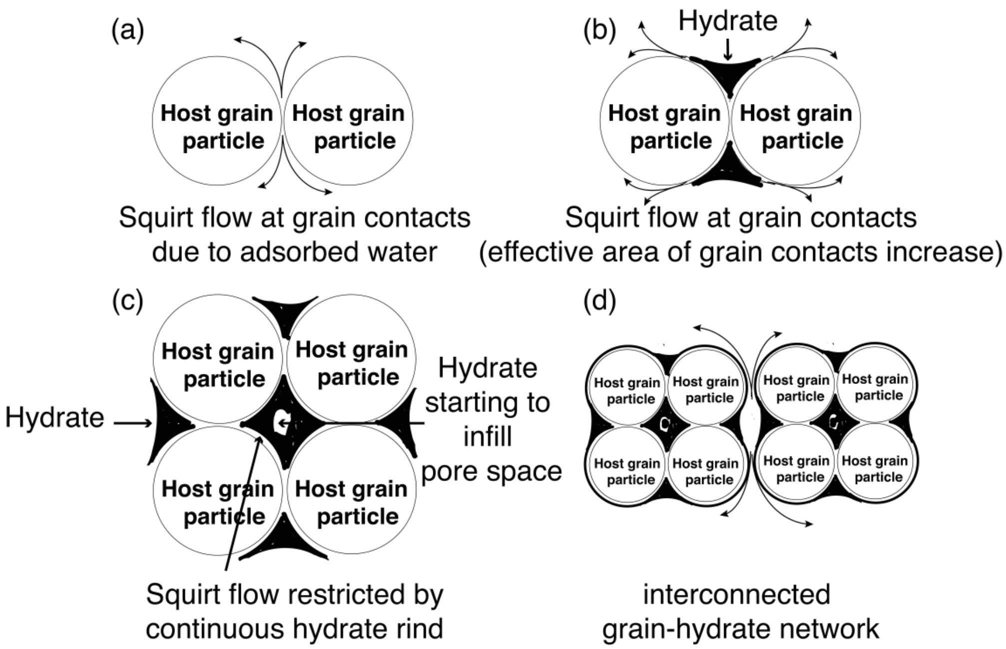

Figure 15. Conceptual model of cementing hydrates growing at grain contacts with increasing gas hydrate saturation. (a) Host grains without hydrates; (b) Hydrates growing at grain boundaries; (c) Enveloped grains with hydrates; (d) Interconnected grain-hydrate network (Modified after Priest et al., 2006).

737x477mm (600 x 600 DPI)

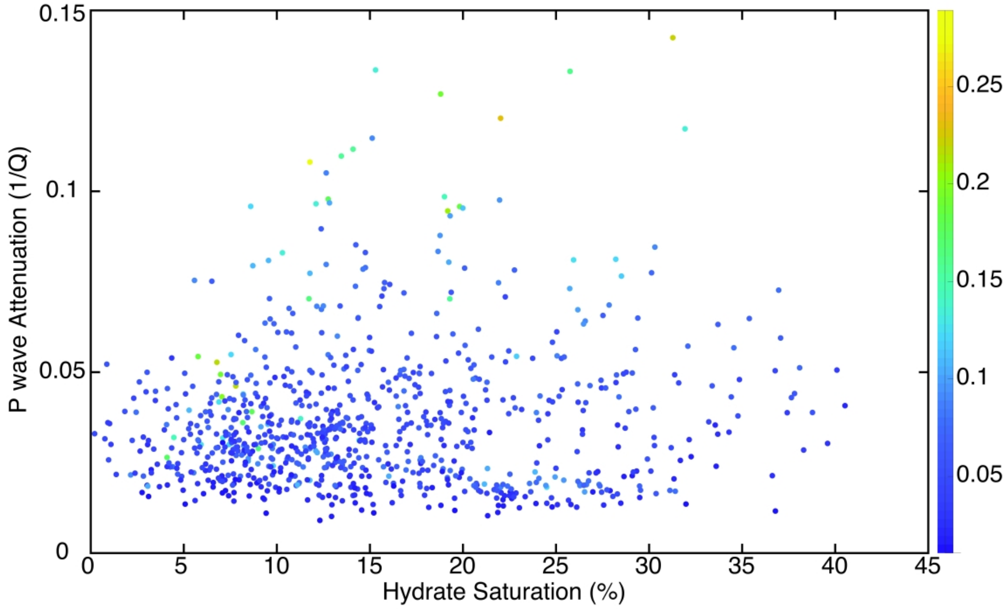

Figure B1. Scattering plot of the seismic attenuation and gas hydrate saturation above the BSR from 1244E, 1247B and 1250F. Different colors represent the standard deviation of P wave attenuation.

881x538mm (600 x 600 DPI)

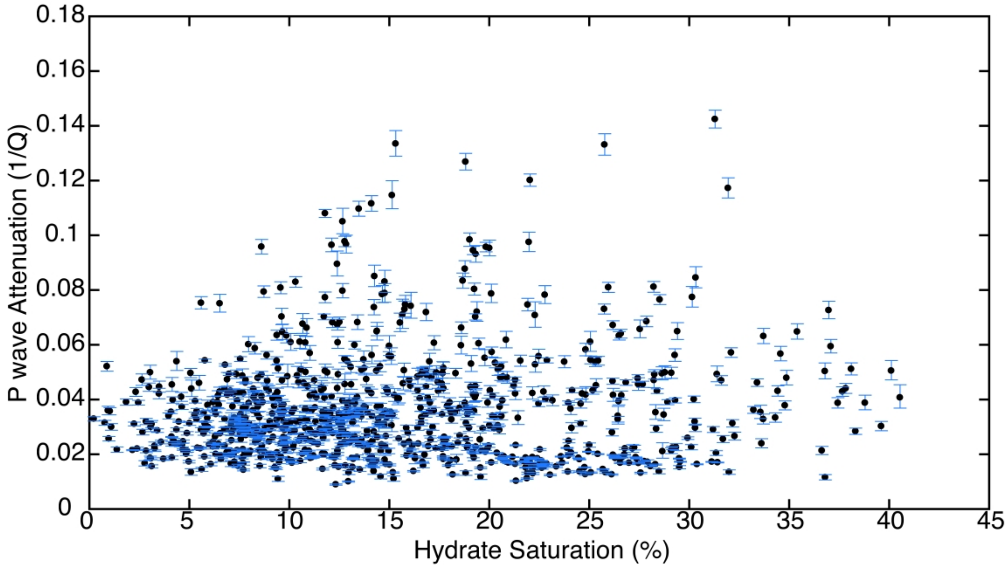

Figure B2. Measured mean attenuation (dots) with error bar showing the 95% confidence interval as a function of hydrate saturation.

838x479mm (600 x 600 DPI)

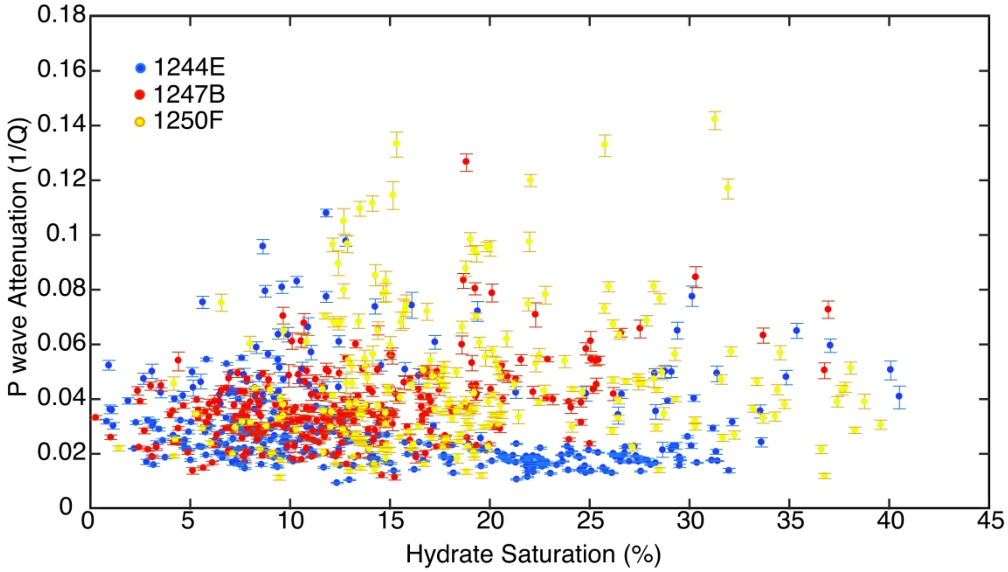

Figure B3. Measured mean attenuation (dots) with error bar showing the 95% confidence interval as a function of gas hydrate saturation for 1244E, 1247B and 1250F, respectively.

839x482mm (600 x 600 DPI)

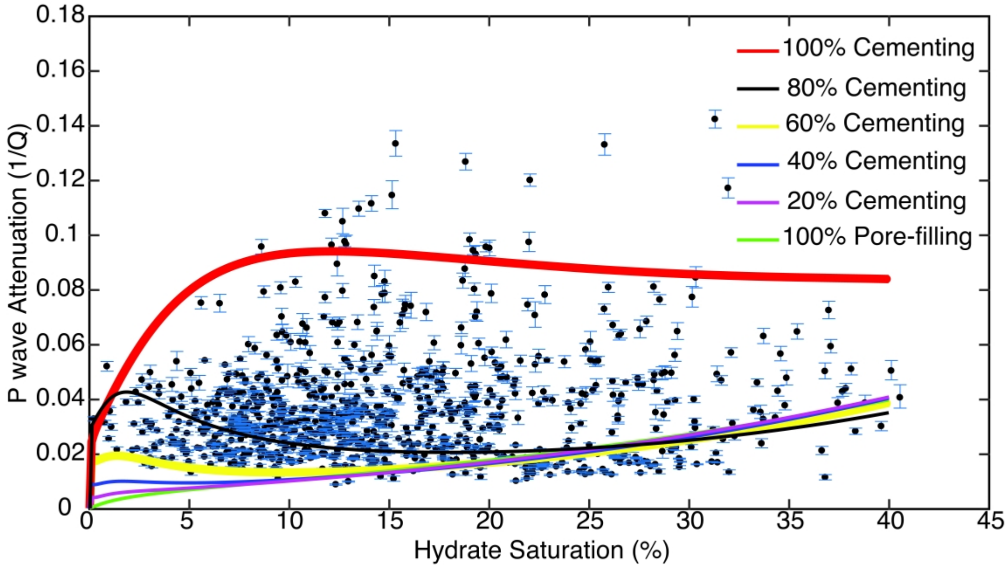

Figure B4. Measured mean attenuation (dots) with error bar showing the 95% confidence interval and modeled attenuation (lines) as a function of gas hydrate saturation.

838x479mm (600 x 600 DPI)

Table 1. Published and this study's seismic attenuation (Q value is the inverse of the attenuation) for hydrate-bearing sediments.

Location	Frequency (Hz)	Q value	Saturation
Blake Ridge, US (Wood et al., 2000)	20-150 (Single-channel)	200-300	3%-4%
	10-120 (VSP)	>20	
	10k-20k (Sonic logging)	No data	
Mallik field, Canada (Dvorkin & Uden 2004, Bauer et al., 2008)	10k-15k (Sonic logging)	6-20	60%-80%
	10-200 (VSP)	7-13	
	150-500 (Crosshole)	5-11	
Nankai Trough, Japan (Matsushima et al., 2006)	10k-20k (Sonic logging)	25-100	20%-30%
	30-110 (VSP)	>100	
Western Svalbard, Norway (Madrussani et al., 2010)	20-200 (3D seismic)	150-200	6%-10%
Krishna-Godavari, India (Nittala et al., 2017)	8k-15k (Sonic logging)	344.82	50%-80%
	5-50 (3D seismic)	80-81	
	5-120 (Multi-channel at 01-10 site)	160-320	
Gulf of Mexico (Wang et al., 2017)	8k-24k (Sonic logging)	50	40%-75%
Cascadia, Oregon (this study)	25-200 (3D seismic)	>50	8%-10%
	30-150 (VSP)	>80	
	3k-15k (Sonic logging)	>90	

Table C1. Fixed input parameters used in the HBES model.

Parameter	Value	Unit	Reference
Confining pressure (P_c)	1.14×10^7	*Pa*	
Pore fluid pressure (P_p)	0.92×10^7	*Pa*	
Temperature (T)	9	℃	
Hydrate bulk modulus (K_H)	7.9×10^9	*Pa*	(Best et al., 2013)
Hydrate shear modulus (G_H)	3.3×10^9	*Pa*	(Best et al., 2013)
Hydrate Possion's ratio (ν_H)	0.32		(Marín-Moreno et al., 2017)
Hydrate Density (ρ_H)	925	*Kg/m³*	(Helgerud et al., 2009)
Methane bulk modulus (K_{CH_4})	$K_{CH_4}(P_p, T)$	*Pa*	(Millero et al., 1980)
Methane density (ρ_{CH_4})	$\rho_{CH_4}(P_p, T)$	*Kg/m³*	(Millero et al., 1980)
Methane viscosity (μ_{CH_4})	$\mu_{CH_4}(P_p, T)$	*Pa s*	(Millero et al., 1980)
Methane irreducible saturation (S_{rCH_4})	0.02		(Reagan and Moridis, 2008)
Grain bulk modulus (K_s)	36×10^9	*Pa*	(Ecker et al., 2000)
Grain shear modulus (G_s)	45×10^9	*Pa*	(Ecker et al., 2000)
Grain Poisson's ratio (ν_s)	0.062		(Marín-Moreno et al., 2017)
Grain density (ρ_s)	2650	*Kg/m³*	(Ecker et al., 2000)
Grain diameter (d_s)	1×10^{-4}	*m*	(Best et al., 2013)
Grain coordination number (n)	8.5		(Ecker et al., 2000)

Water bulk modulus (K_W)	K_W (P_p, T)	*Pa*	(Setzmann and Wagner, 1991)
Water density (ρ_W)	ρ_W (P_P, T)	Kg/m^3	(Setzmann and Wagner, 1991)
Water salinity (s)	3.5	*% wt*	
Water irreducible saturation (S_{rW})	0.2		(Reagan and Moridis, 2008)
Porosity without hydrate (φ_0)	0.40		(Daigle et al., 2015)
Critical porosity (φ_c)	0.38		(Best et al., 2013)
Intrinsic permeability without hydrate (K_0)	10^{-13}	m^3	(Daigle et al., 2015)

Table C2. Case dependent input parameters used in the HBES model.

Parameter	Value	Unit	Reference
Aspect ratio of inclusions containing methane or water	$\alpha\{iCH_4, iW\}$		
Concentration of cementing hydrate (C) and pore-filling hydrate (PF)	$c\{C,PF\}$		
Concentration of inclusions in hydrate	c_i	Pa	
Frequency	f	Hz	
Porosity	φ		
Saturation of hydrate, methane, and water in the pore space	$S\{H, CH_4, W\}$		

DATA AND MATERIALS AVAILABILITY

Data associated with this research are available and can be obtained by contacting the corresponding author.

DOI:10.1190/int-2020-0137.1